

Cepheid Variable Stars in Globular Cluster NGC 1866

Thesis
submitted in partial fulfilment
of the requirements for the
degree of
MSc Astrophysics
Liverpool John Moores University, 2019

C. E. BRASSEUR

ABSTRACT

Cepheid stars are one of the most important classes of variable star due to their well defined period-luminosity and period-age relations. Their high luminosity combined with the period-luminosity relation makes them one of the most commonly used primary distance indicators over a range of galactic and extragalactic scales (Bono et al. 2005; Marconi et al. 2013). Additionally, their period-age relation allows Cepheids to be used as stellar evolutionary tracers in the Milky Way and nearby galaxies (Magnier et al. 1997). In this study I explore the Cepheids of the Large Magellanic Cloud (LMC) open cluster NGC 1866, detecting the variable stars, and determining their periods. I use independent data to determine the age of the cluster using main sequence turn-off fitting, and combine the results with measurements from other LMC clusters to derive a period-age relation. I compare my results with literature values and discuss complicating factors.

Contents

1. Introduction	3
2. Background	3
3. Methods	5
3.1. Data	5
3.2. Variable star detection	6
3.3. Period analysis	11
3.4. Age determination	14
3.5. Period-Age Relation	16
4. Discussion	18
4.1. NGC 1866 Cepheid Population	18
4.2. NGC 1866 cluster age and distance	20
4.3. Cepheid period-age relation	21
5. Conclusion	23
A. Detected Cepheid Periods	26
B. Detected Cepheid Phased Light Curves	27

1. INTRODUCTION

Cepheid stars are a class of regularly pulsating star with well defined relationships between period, luminosity, and age, making them useful in the estimation of cosmic distances, and for tracing young stellar populations (Bono et al. 2005; Musella et al. 2016; Soszyński et al. 2015). Globular clusters offer the opportunity to study a population of Cepheid stars all with the same distance, age, and chemical composition, useful for tuning the empirical period-luminosity and period-age relations, particularly when there are independent distance and age measurements to compare to (Bono et al. 2005). In this paper I focus on the Large Magellanic Cloud (LMC) open cluster NGC 1866, which is particularly rich in Cepheids stars, hosting at least 22 known Cepheid variables.

Using ground-based photometry from the Las Cumbres Observatory (LCO) taken over the course of four months, I identify variable stars in NGC 1866, extract their light curves, and perform period analysis, ultimately obtaining a sample of detected variable sources and their periods. Independently, using photometry from the Hubble Space Telescope (HST), I obtain distance modulus and age estimates for the cluster by comparing observational data with model isochrones. Finally, I combine these results with results from other LMC clusters to derive an estimate of the Cepheid period-age relation, and compare to literature values. In §2 I motivate this work, §3 details the data reduction and analysis, in §4 I compare my results to previous studies, and §5 concludes.

2. BACKGROUND

Classical Cepheids (also called δ Cephei stars or type I Cepheids) are young, luminous, supergiant stars with typical ages < 400 Myr and luminosities in the range $100 - 10,000L_{\odot}$ (Skowron et al. 2019). They are variable stars that pulsate with periods on the order of 1-100 days and have a characteristically saw-tooth shaped light curve (Skowron et al. 2019). Cepheids follow both a period-luminosity relation (first described by Leavitt & Pickering (1912)) and a period-age relation (first derived by Young (1962)).

Classical Cepheids play an important role in both galactic and extragalactic astronomy. Because of their intrinsic brightness they can be detected in both our own galactic disk and external galaxies, and because of their well constrained period-luminosity and period-luminosity-colour relations they make excellent distance indicators (Bono et al. 2005). Their period-age and period-age-colour relations can be used to trace stellar age distributions (e.g. Magnier et al. (1997)), as well as for refining stellar evolution and pulsation models, particularly in young stellar populations (Soszyński et al. 2015).

Cepheids occupy the classical instability strip of the Hertzsprung-Russell (HR) diagram, as shown in Figure 1. They are evolved (post-hydrogen burning) intermediate mass stars whose progenitors were hot B-type stars with masses in the range

$\sim 3 - 12M_{\odot}$, typically with spectral types above B5 (Anderson et al. 2016). Cepheids themselves are slowly rotating yellow supergiants with expanded envelopes having radii between $\sim 20 - 200R_{\odot}$ that are evolving through a number of short evolutionary stages on the way to becoming red supergiants. Cepheid stars will typically pass through the instability strip multiple times as core helium burning stars, and then later as shell helium burning stars (Turner 2012).

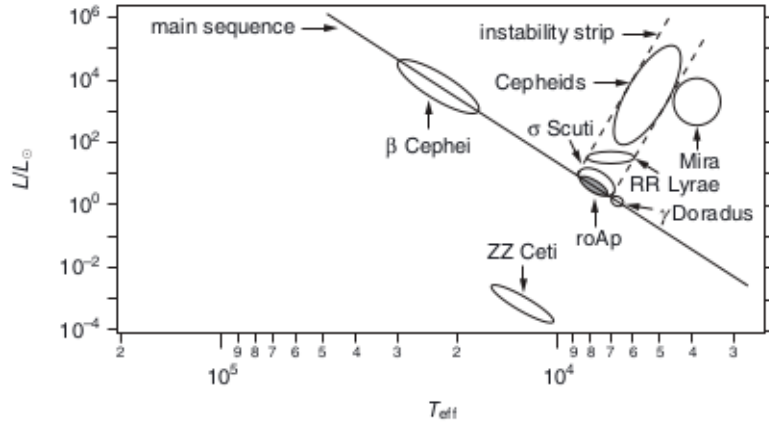


Figure 1. LeBlanc (2010)'s figure 5.11, a Hertzsprung-Russell (HR) diagram showing the location of different classes of variable star, including Cepheids, in relation to the main sequence line.

NGC 1866 is a young globular cluster in the LMC that is particularly rich with Cepheid variable stars, boasting more than 20 known examples (Welch & Stetson 1993; Musella et al. 2016). Stellar clusters like NGC 1866 offer the opportunity to study a population of stars all of the same distance and age, and with reasonably homogeneous chemical composition (Musella et al. 2016). NGC 1866 is of particular interest because it is well populated in both the main-sequence and post main-sequence stages of stellar evolution, allowing for the exploration of objects across evolutionary stages, and thus the testing of stellar evolutionary models (Barmina et al. 2002).

The presence of so many Cepheid stars in a single cluster offers a unique opportunity to explore empirical and theoretical estimates for the relationship between colour, luminosity, and period (Musella et al. 2016). Additionally, the observation of Cepheids in several such clusters offers the opportunity to calibrate the Cepheid period-age and period-age-colour relations (Bono et al. 2005). Because this relation allows Cepheid ages to be determined individually, they can be used to trace populations of different ages, and explore the so called “galactic texture,” the distribution size and age range of stellar groupings in galaxies (Magnier et al. 1997). Skowron et al. (2019) used the Cepheid period-luminosity and period-age relations together to construct a map of the Milky Way in three dimensions plus age distribution, allowing them to compare their observations to galactic evolution simulations.

3. METHODS

I used difference imaging to detect the variable sources present in NGC 1866, extracted light curves from the photometry for those variable sources, and then performed period analysis on the results. This part of the analysis is described in §3.2 and §3.3. Independently, I compared photometric measurements of stars in NGC 1866 to model isochrones to determine the age of the cluster, described in §3.4. Finally, I combined these results to explore the period-age relation of Cepheid variable stars (§3.5). My data tables and analysis code are available on github (github.com/ceb8/CepheidVariables).

3.1. Data

For the detection and characterisation of individual Cepheid variables in NGC 1866, I used photometric data in the I- and V-bands taken at the Las Cumbres Observatory (LCO) at Sliding Spring in New South Wales, Australia over the course of several months, from October 2015 through February 2016. The data was taken in 30 second exposures, on a 2-metre Ritchey-Chrétien Cassegrain telescope, fitted with a 4K x 4K 15-micron spectral camera. The two filters I used were the Bessell V filter ($\sim 5000 - 5900\text{\AA}$) and the Bessell I filter ($\sim 7200 - 8800\text{\AA}$). All of the data was processed through LCO’s ORAC-DR data reduction pipeline¹ which includes bad-pixel masking, bias subtraction, dark subtraction, and flat field correction. I had 34 images in each band, although a few were obscured by clouds and unusable. The final count of images I was able to successfully use for period detection was 27 V-band images, and 24 I-band images.

I used the PARSEC isochrones v1.2s, generated by CMD version 2.7² ([Bressan et al. \(2012\)](#), [Chen et al. \(2014\)](#), [Tang et al. \(2014\)](#)) in combination with Hubble Space Telescope (HST) wide-field camera 3 (WFC3) observations of NGC 1866 for my age determination analysis. I used two HST/WFC3 filters, the UVIS wide filter F438W which corresponds to $\sim 4000 - 4750\text{\AA}$, the B-band, and the UVIS wide filter F555W which corresponds to $\sim 5500 - 7250\text{\AA}$, the V-band³. This data was taken as part of the on-going Large/Small Magellanic Cloud HST survey of massive stellar clusters described in [Niederhofer et al. \(2017\)](#). The WFC3 images were processed through the standard HST pipeline, corrected for imperfect charge transfer efficiency, calibrated for bias, dark, low-frequency flats and improved UVIS zero-points. The stellar photometry was derived using point-spread function (PSF) fitting methods with spatially variable “effective PSF” libraries developed by [Anderson & King \(2006\)](#). These magnitudes were then transformed into the VEGAMAG system and aperture correction applied ([Niederhofer et al. 2017](#)).

¹ lco.global/documentation/data/ORACpipeline/

² stev.oapd.inaf.it/cmd

³ See the HST WFC3 handbook for filter throughput plots: stsci.edu/hst/instrumentation/wfc3

3.2. Variable star detection

Image subtraction is a technique for finding variable objects in a series of images by subtracting one from another so that changes can be detected. For image subtraction where observational conditions, such as seeing, vary between images, a convolution kernel is used to match the images for subtracting (Alard & Lupton 1998).

Before the image subtraction algorithm can be run, the images to be subtracted must be aligned. I did this in a two step process, first correcting the world coordinate system (WCS) information in each image to match the coordinates given in the Gaia data release 2 catalogue (Gaia Collaboration et al. (2018), Gaia Collaboration et al. (2016)), and then re-sampling all images onto a common grid, an arbitrarily chosen V-band image.

I used Clare Shanahaan’s WCS correction code⁴, which takes a matched set of sky positions (right ascension/declination), and x/y pixel coordinates, and produces the best fit tangent projected WCS object. I obtained the matched sky position, pixel coordinate pairs by using seven bright stars that were easy to pick out in each image. I noted the sky positions of those coordinates in the Gaia catalogue (Gaia Collaboration et al. 2018), and then used the DAOFIND algorithm with a high threshold to extract the pixel locations of the brightest stars in each image (Craig et al. 2015). I could then use Astropy’s catalogue matching functionality to get the most likely correspondence between the Gaia sources and the DAOFIND detected bright sources. I checked the result of this step manually and tuned the DAOFIND threshold as necessary (see Figure 2 top left).

The resulting paired sky positions and pixel coordinates were then run through Shanahaan’s function to obtain a corrected WCS object. I checked this result by using the newly created WCS to find the sky position of every source detected by DAOFIND, and then cross-matching the result with the list of Gaia sources present in the image. I then produced a histogram of the result with the approximate full-width half-max (FWHM), or expected error in source position pixel value, marked (see Figure 2 bottom). If nearly all separations between the Gaia and WCS calculated positions were smaller than the FWHM, the WCS was considered correct. A few sources with large separations were expected, due to the Gaia source list containing some sources too faint to be seen in the Las Cumbres images, and thus being incorrectly matched with the nearest sources there were visible. Images that were of noticeably lower quality resulted in more of these outliers. As a final check I used the corrected WCS to find the pixel coordinates of the Gaia sources and over-plotted them on the image, checking manually to see that they were indeed over real sources (see Figure 2 top right).

Once I had good WCS information for all the images, I projected each image onto a single arbitrarily chosen V-band image. To do this I used the reproject Python

⁴ Part of a forthcoming addition to the Astropy package: github.com/astropy/astropy/pull/7884

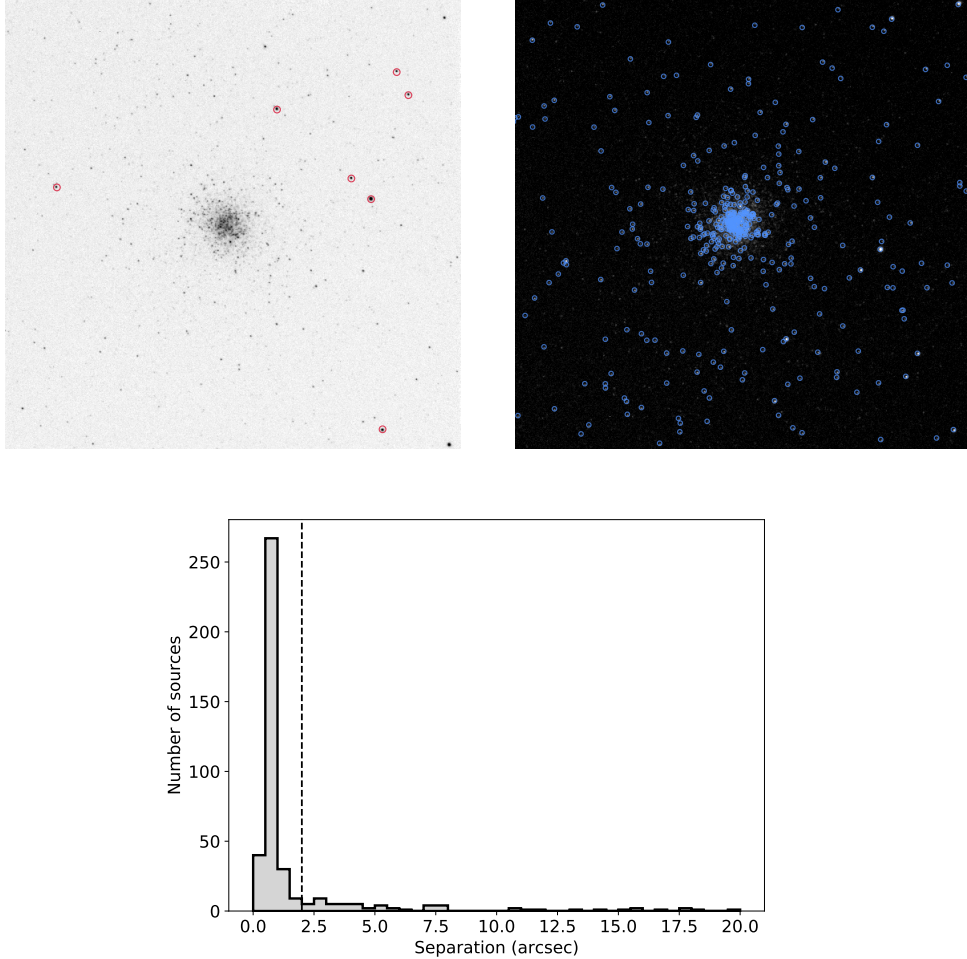


Figure 2. WCS correction and source matching. The upper left image shows the fixed stars I used to correct the WCS information, the upper right shows Gaia sources over-plotted using the corrected WCS, and the bottom histogram quantifies the separation between Gaia sources and image sources using the corrected WCS. The vertical dotted line marks the approximate FWHM, which is the expected uncertainty in source position.

package to resample the images onto a single WCS and footprint, using bilinear interpolation (Robitaille 2018). Figure 3 shows two images before and after alignment.

Once all of the images were properly aligned I created a template image in each bandpass to use as the reference image for the image subtraction step (the image from which I would subtract all the other images). I used DS9 (Joye & Mandel 2003) and imexam (Sosey 2017) to manually inspect all images and choose the best ones, defined as those with good seeing, low FWHM, and low sky background. I chose 7 V-band images, and 6 I-band images to create a deep template image in each band. I combined the individual exposures into the template image using the Python package ccdproc (Craig et al. 2015) to both combine the images and perform cosmic ray rejection. To remove the cosmic rays I performed sigma clipping, removing all values more than 2.5σ from the image median. I applied this algorithm iteratively until no more values were rejected. After the cosmic ray rejection, I combined the images by taking the

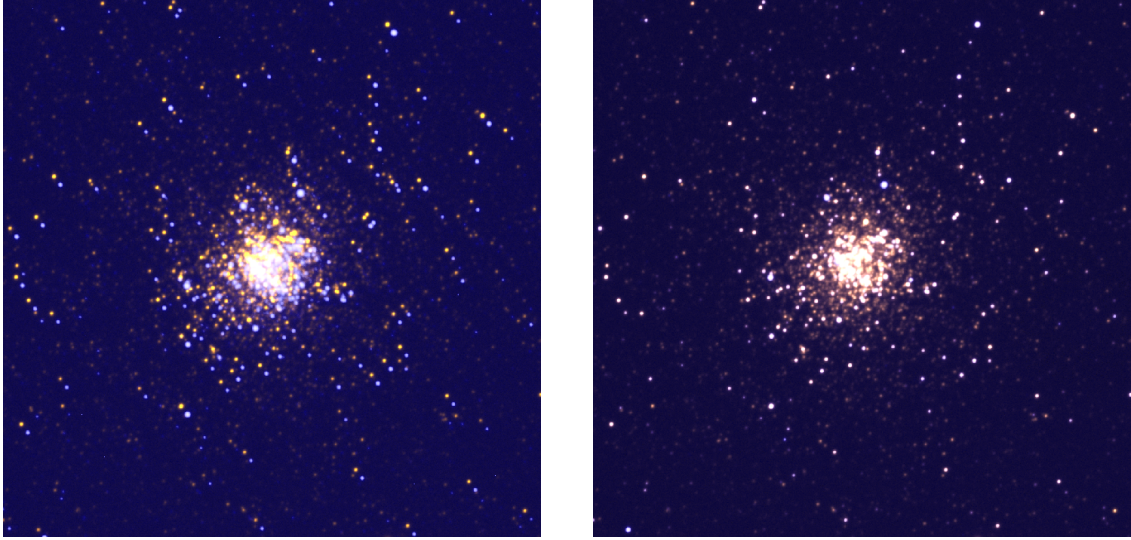


Figure 3. Two images of NGC 1866, rendered in colour and zoomed in to demonstrate the transition, before (*left*) and after (*right*) alignment.

average of the images excluding the pixels rejected in the previous step. Figure 4 shows the template images for both bands.

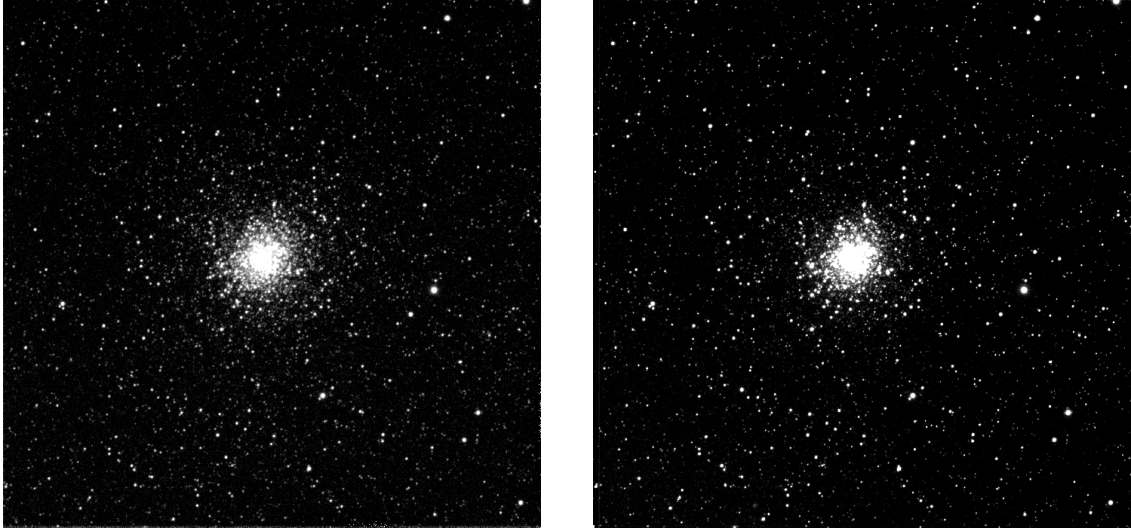


Figure 4. Template images for V-band (*left*) and I-band (*right*).

After creating the image templates, I used the High Order Transform of Psf ANd Template Subtraction code (hotpants) software, version 5.1.11 (Becker 2015), to perform the image subtraction. Hotpants implements the Alard (2000) algorithm for image subtraction using a space varying kernel. The basic technique for image subtraction is to select a reference image, usually the image with the best seeing or a co-added image of several particularly good images (as in this study), and convolve the reference image to the seeing of each frame to be subtracted before performing pixel by pixel subtraction. The convolution is performed by using a convolution

kernel. Alard & Lupton (1998) showed that the optimal kernel for this operation is a space varying kernel that satisfies the least-squares solution of the equation

$$\text{Ref}(x, y) \otimes \text{Kernel}(u, v) = I(x, y) \quad (1)$$

where Ref is the reference image, Kernel is the kernel, and I is the image whose seeing is being matched. The particular algorithm used in the hotpants software is described in Alard (2000) and involves approximating the image noise with Gaussian distributions to allow the problem to be expressed as a linear least squares problem. In this way I was able to use my reference images to obtain difference images for each observation. There were 6 V-band images and 7 I-band images where the image subtraction failed, so at the end of this step I had 27 V-band difference images and 24 I-band difference images to use in detecting and analysing the periodic sources.

The images that failed the image subtraction step were ones where the background flux was high, the dynamic range was low, and the PSF was large. Figure 5 shows two V-band images, one that succeeded in image subtraction (*left*) and one that failed (*right*), both shown with the same scaling parameters. We can see that the image on the right is much blurrier, and the background shows much higher noise. Additionally the flux values in the left have a range of ~ 4150 while the image on the right only has a range of ~ 720 . This is only one example, but the general features are true of all the images that failed image subtraction.

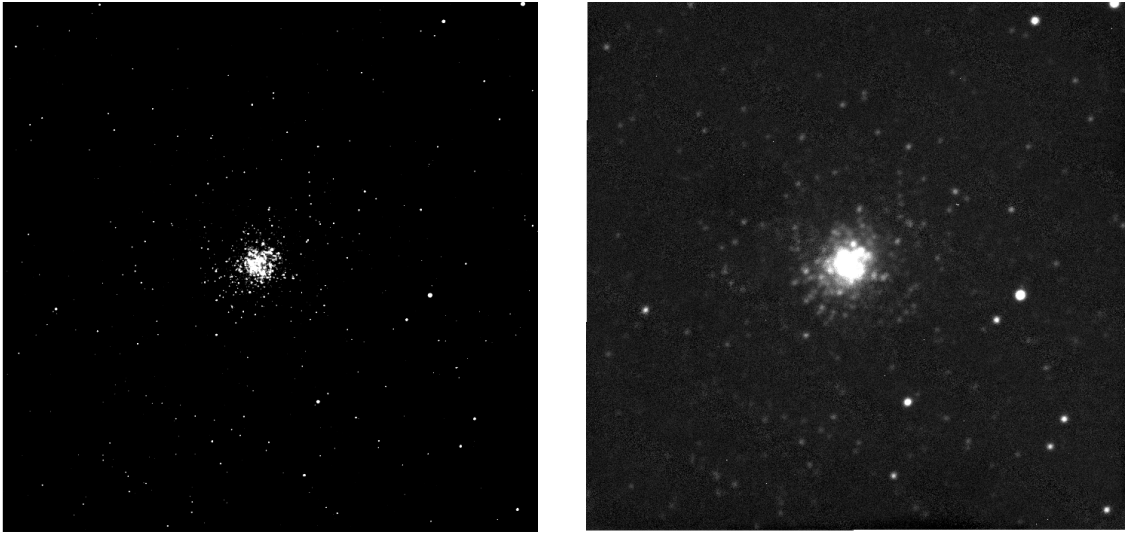


Figure 5. Two V-band images, one that succeeded in image subtraction (*left*) and one that failed (*right*).

Once I had my collection of difference images, I inspected them manually, picking out the four best images in each bandpass, where “best” is defined as minimal variation in the background, low FWHM, and minimum residuals from bright stars. I took these images and stacked them, after taking the absolute value of each image,

so that the variable sources would be more visible. I ran the DAOFLIND algorithm for detecting sources in a crowded field on the stacked difference images (Stetson 1987). Figure 6 shows the detected sources on the stacked images. There are clearly some mis-detections, particularly in the I-band at the edges of the image, however most of the detections look reasonable.

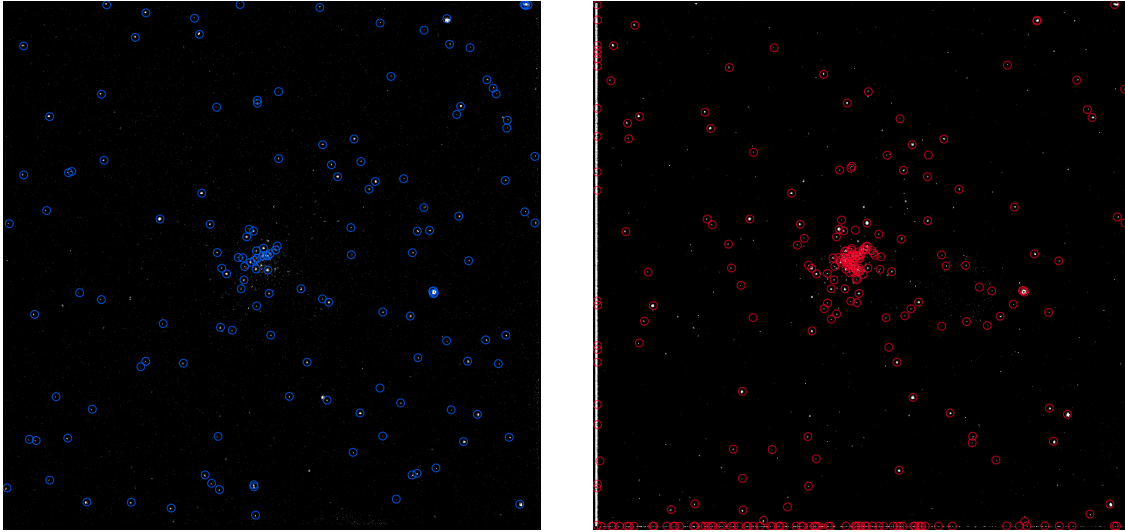


Figure 6. Stacked difference images and detected sources for V-band (*left*) and I-band (*right*).

I also ran the DAOFLIND algorithm on the V-band template image to get a list of all visible sources to provide a sanity check on the variable sources found in the difference stacks. I cross-matched all three catalogues to get my final list of variable source detections. Figure 7 *left* shows the detections in the two bands as blue (V-band) and red (I-band) dots overlaid on the original NGC 1866 image, with the detections in both bands appearing purple. The final set of 50 detected variables are shown on the right, these are all the detected sources where the V-band and I-band catalogues, both had sources within 0.0005° (1.8 arcsec) of a template source. This separation was chosen to be the approximate FWHM of the images. By restricting my sample to sources detected in both bands, I lose any sources that are truly variable but not observable in the I-band, which is a possibility as Cepheid stars are generally fainter in the I-band than the V-band.

I next extracted light curves for each star in my final table of variable sources. To do this I performed aperture photometry using the photutils Python package on every detected variable in each difference image (Bradley et al. 2016). Because I performed the photometry on difference images, the result is the measurement of the difference between the flux in the given observation and the flux in the template image. I have not corrected the flux values based on the flux in the template images.

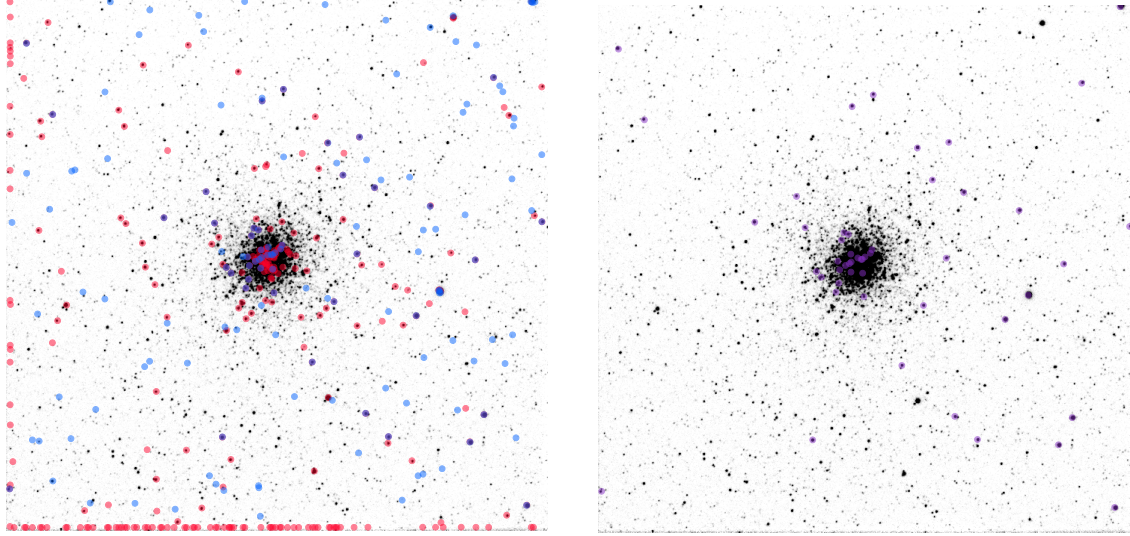


Figure 7. Variable source detections in the V-band (blue) and I-band (red), with the overlap shown in purple. All detections are shown on the left, and only the ones present in both bands and the template are shown on the right.

3.3. Period analysis

To determine the periods of the variable stars, I constructed a Lomb-Scargle periodogram for each light curve. I used the Lomb-Scargle implementation in the Astropy Python package, which implements the methods described in VanderPlas et al. (2012) and VanderPlas & Ivezić (2015). In building the frequency grid, I took into account the considerations for unevenly sampled data described in VanderPlas (2018), specifically the discussion of non-uniform Nyquist limits in §4.1, and frequency grid spacing in §7.1. Given that the observational spacing of my data is arbitrary, I cannot use it to estimate the Nyquist limit, so instead I considered the temporal precision and integration time. The temporal precision of the observations is 7 decimal places, making the Nyquist limit $f_{Ny} \leq \frac{1}{2}10^7 \text{ days} = 5,000,000 \text{ days}^{-1}$. This is a far higher Nyquist limit than is practicable to compute. Turning instead to the frequency limit imposed by the 30 second integration time yields a maximum frequency $f_{max} \propto \frac{1}{2(30\text{sec})} = 1440 \text{ days}^{-1}$. While this is more reasonable, it is still a higher frequency limit than makes sense for this problem. So instead of considering the characteristics of my data I considered instead the characteristics of the problem. I am characterising the periods of Cepheid variable stars, stars which have periods that generally fall in the range of 1-100 days. Thus the maximum frequency we would expect to see would be 1 day^{-1} . I relax this slightly since it isn't an exact period range and take the value $f_{max} = 2 \text{ days}^{-1}$. Because the frequency range is not too wide, I chose a generous samples-per-peak value of $n_o = 10$ and combined this with the total observation window of $T = 134$ days to calculate the total number of periodogram evaluations as $N_{eval} = n_o T f_{max} = 2680$. I thus used a frequency grid of 2,680 frequencies evenly spaced between 0 and 2 days^{-1} . Figure 8 shows two examples of Lomb-Scargle periodograms of my light curves, the top plot is an example

where there is a clear dominant frequency, and some aliasing of those peaks, while the bottom plot shows a more noisy spectrum that does not show as much structure.

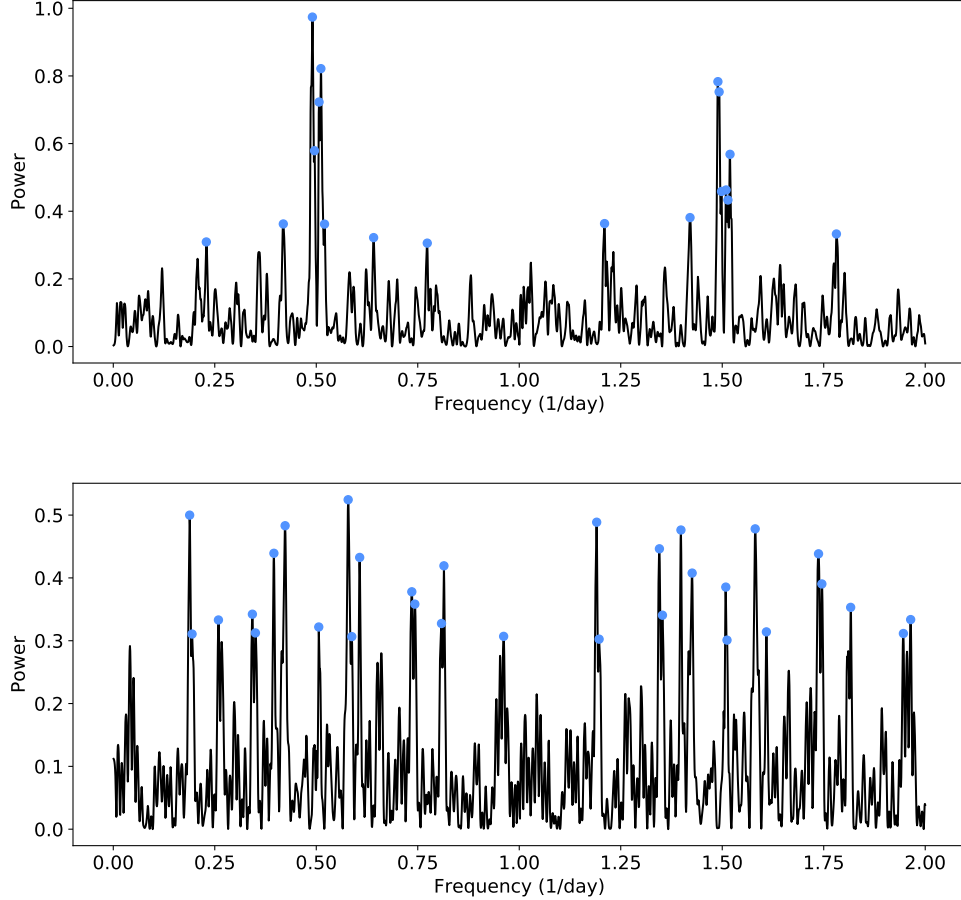


Figure 8. Lomb-Scargle periodograms for two light curves. The peak frequencies tested are marked with blue dots. The top periodogram shows a clear peak, and some aliasing. The bottom periodogram has less obvious structure.

One of the challenges with period finding on unevenly sampled data is that the interaction between the window function, the underlying periodic function, and the noise in the data make it quite likely that the largest peak in the periodogram does not actually correspond to the true frequency of the data, but to some alias of that frequency. Instead of treating this in an analytic manner, I simply scored all frequencies with powers over 0.3⁵ using the Analysis Of Variance scoring algorithm (Schwarzenberg-Czerny 1989). The specific implementation I used was that from the VARTOOLS Light Curve Analysis Program, which I ported into Python (Hartman & Bakos (2016); Devor (2005)).

⁵ Standard normalisation was applied to the Lomb-Scargle powers, see:
docs.astropy.org/en/stable/timeseries/lombscargle.html#standard-normalization

In this way I determined the best period for each star in both the V- and I-bands. I determined the final best period for each star by taking the best scoring period between the V- and I-bands. Not all of the period detections were compelling; I manually examined the results and applied a scoring threshold of -5 (lower scores indicate stronger periodicity) bringing the number of variable detections down from 50 to 27 with sufficiently good period determinations. Figure 9 *top* shows an example of a light curve that did not meet the threshold requirements for the final period determination. The plot shows no strong trend across the phase, with the points more or less scattered randomly across the flux range. Figure 9 *bottom* shows a light curve that did pass the scoring threshold, periodicity is clearly visible in this light curve. At 51.5 days, the plot in Figure 10 is a definite outlier in the detected periods, an indication that the detected period may be an alias of the true period. A table of all detected Cepheids and their periods is available in Appendix A, and the phase plots of all the light curves are shown in Appendix B. With one exception all the detected periods fall between $\sim 0.5 - 3.5$ days (see Figure 11), this is a plausible period range for Cepheid stars.

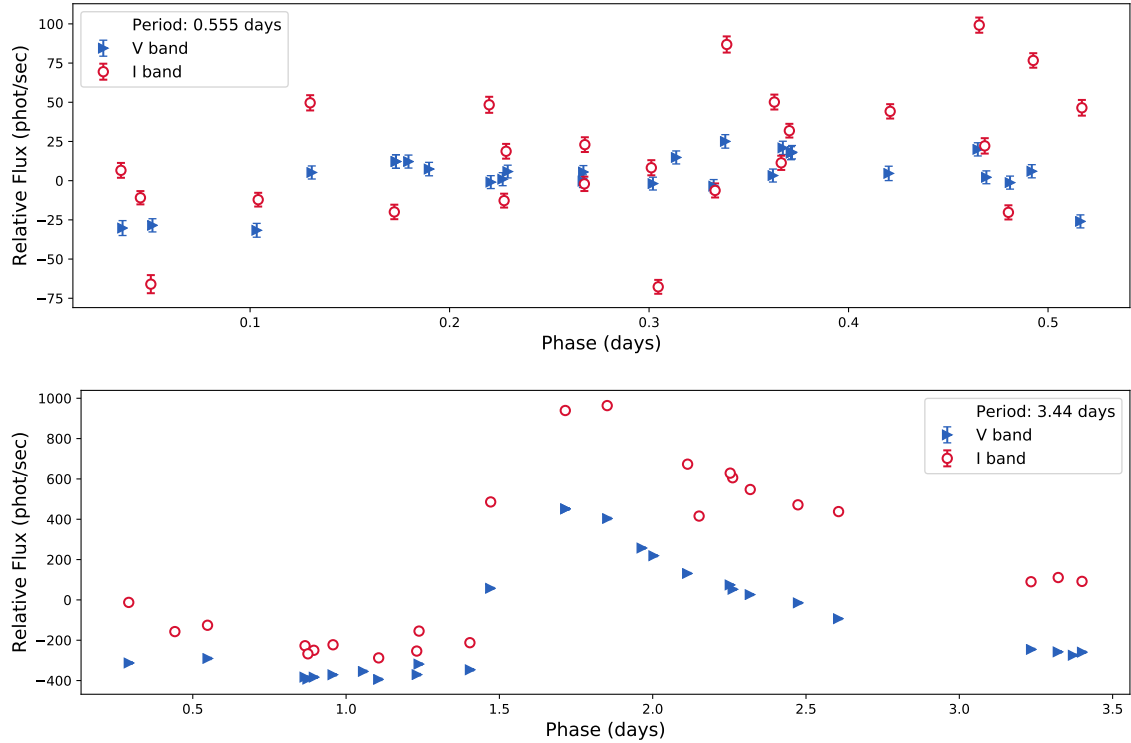


Figure 9. Two phased light curves, one that did not pass the periodicity threshold (*Top:*) and one that did (*Bottom:*).

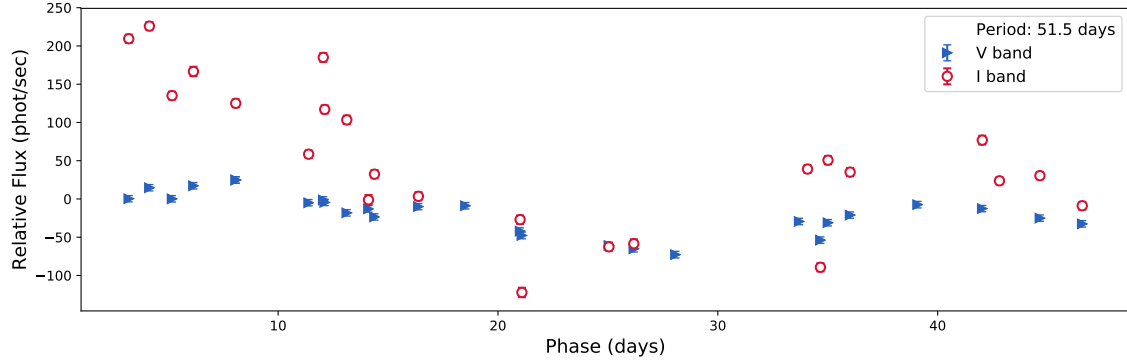


Figure 10. The phased light curve with the longest period (51.5 days).

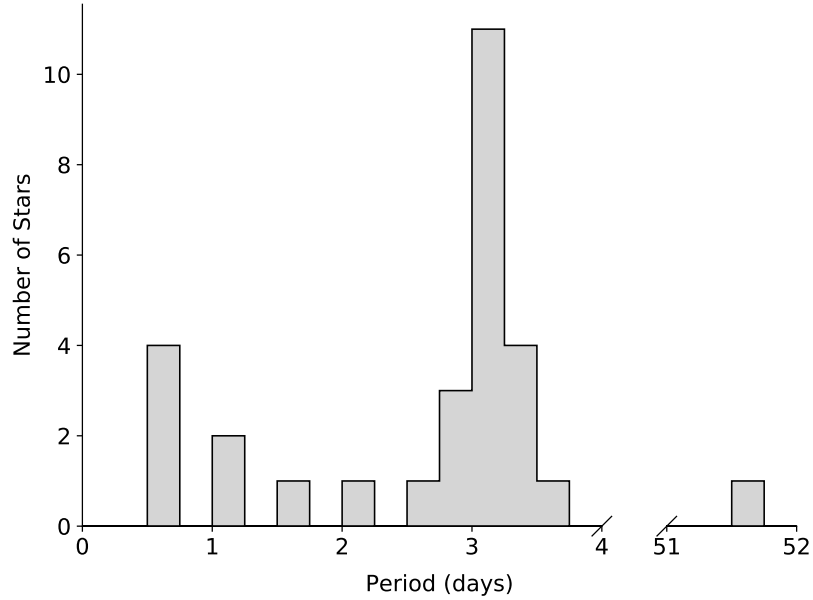


Figure 11. Histogram of the detected periods, note the break in the x-axis.

3.4. Age determination

To determine the age of the NGC 1866 cluster, I compared photometric data from the Hubble Space Telescope (HST) wide-field camera 3 (WFC3) to model isochrones that simulate the absolute magnitude in the different WFC3 filters for stars with a range of initial properties at different ages. I considered measurements in the F555W (V-band) and F438W (B-band) WFC3 filters, plotting F438W vs. (F438W - F555W) to make a B vs. (B-V) colour-magnitude diagram. However, before I could compare my data to the model isochrones I needed to determine the corresponding apparent

magnitude from the model isochrone absolute magnitudes. To do this I started with the distance modulus (DM),

$$DM = m - M - A \quad (2)$$

where M is the absolute magnitude, m is the apparent magnitude, and A is the extinction value. I treated both the extinction value and the distance modulus as free parameters to be fit, but I fixed the relation between the extinction values in the two filters to the standard value $A_B = 1.33 * A_V$ ([Fitzpatrick 1999](#)). Thus I have the following system of equations to fit:

$$\begin{aligned} m_B &= M_B + DM + A_V * 1.33 \\ m_V &= M_V + DM + A_V \end{aligned} \quad (3)$$

I iterated over DM and A_V values, finding the best fit age for each pair. I determined the fit of an isochrone by computing the distance matrix for each observed magnitude compared to the model isochrone and then calculating the mean squared error for the minimum distance values.

For the first round of fitting I iterated over the ranges

$$\begin{aligned} DM &\in [15, 25] \\ A_V &\in [0, 1]. \end{aligned} \quad (4)$$

This resulted in the mean square error grid shown in Figure 12 *left*, with best fit values

$$\begin{aligned} DM &= 18.5 \\ A_V &= 0.2 \\ \log Age/yr &= 8.15. \end{aligned} \quad (5)$$

I then refined this by taking a finer mesh in the ranges

$$\begin{aligned} DM &\in [18.2, 18.8] \\ A_V &\in [0.1, 0.3]. \end{aligned} \quad (6)$$

which resulted in the mean square error grid shown in Figure 12 *right*, and final fit values

$$\begin{aligned} DM &= 18.68 \\ A_V &= 0.22 \\ \log Age/yr &= 8.1. \end{aligned} \quad (7)$$

The observations and model isochrone are shown in Figure 13.

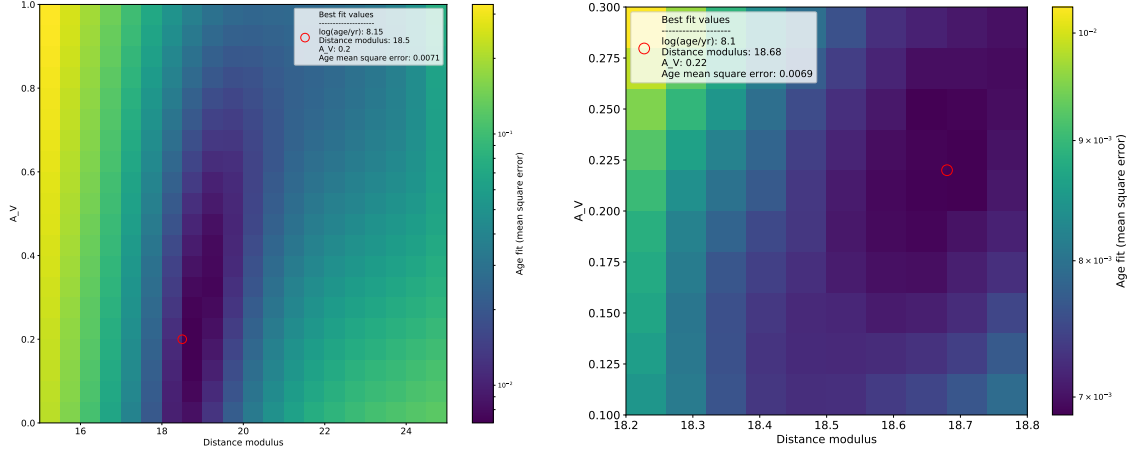


Figure 12. Mean square error grid for different distance modulus (DM) and extinction (A_V) values. The plot on the right shows the grid for a finer mesh around the optimal value identified in the plot on the left.

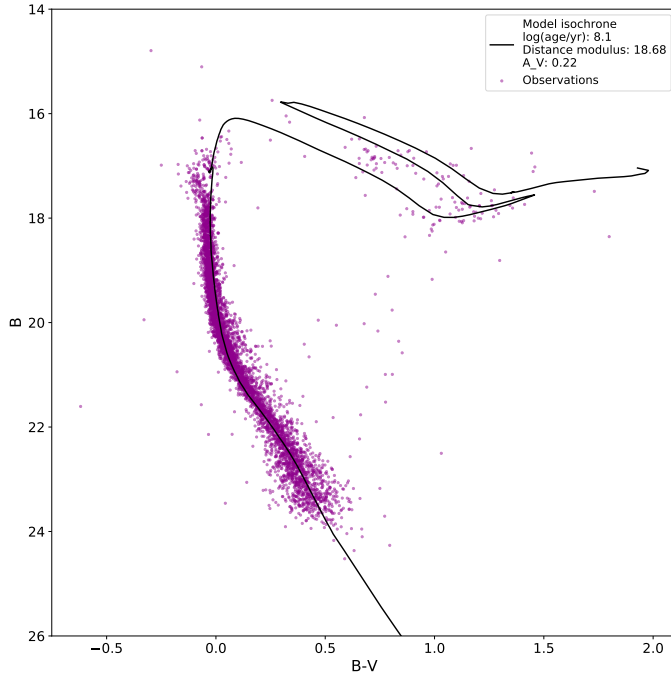


Figure 13. NGC 1866 photometry and best fit model isochrone.

3.5. Period-Age Relation

I combined my period and age findings on NGC 1866 with results from five other clusters to estimate the Cepheid period-age relation. Table 1 contains the information for all six clusters, where the period values were calculated as the mean of all individual Cepheid periods detected in the cluster. The uncertainty in the periods is the standard error of the mean, with the NGC 1818 value showing no error because there was only a single period measurement in that cluster. Previous work (e.g. Bono et al. (2005); Anderson et al. (2016); Efremov & Elmegreen (1998)) leads

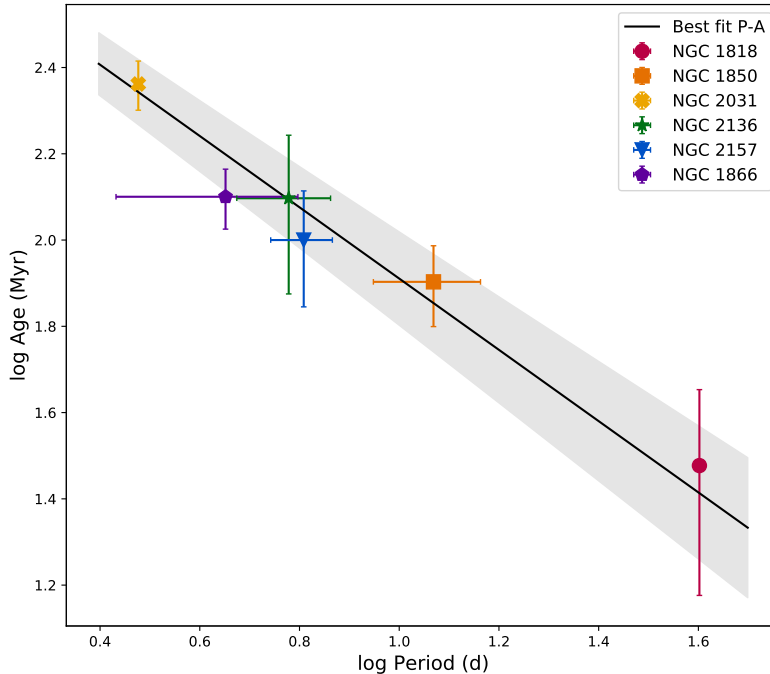
Table 1. Cluster period and age values with associated references.

Reference	Cluster	Period d	Age Myr
This work	NGC 1866	5.146 ± 2.27	141.0 ± 20.0
Ahumada et al. (2019)	NGC 1818	39.999 ± 0.00	30.0 ± 15.0
Milone et al. (2018)	NGC 1850	11.715 ± 2.84	80.0 ± 17.0
L. Short et al, in prep.	NGC 2031	2.997 ± 0.05	230.0 ± 30.0
Niederhofer et al. (2015)	NGC 2136	6.003 ± 1.28	125.0 ± 50.0
Niederhofer et al. (2015)	NGC 2157	6.434 ± 0.91	100.0 ± 30.0

us to expect a relation of the form $\log t = \alpha + \beta \log P$, where t is the age in years and P is the period in days. I used orthogonal distance regression to find the best fit α and β values while taking into account the uncertainties in both period and age. This resulted in the following period-age relation:

$$\log t = (8.74 \pm 0.04) - (0.81 \pm 0.06) \log P. \quad (8)$$

Figure 14 shows the data and best fit line; all points were able to be fit within error margins.

**Figure 14.** Cepheid period-age relation. The black line shows the best fit relation with the one sigma error region.

4. DISCUSSION

4.1. NGC 1866 Cepheid Population

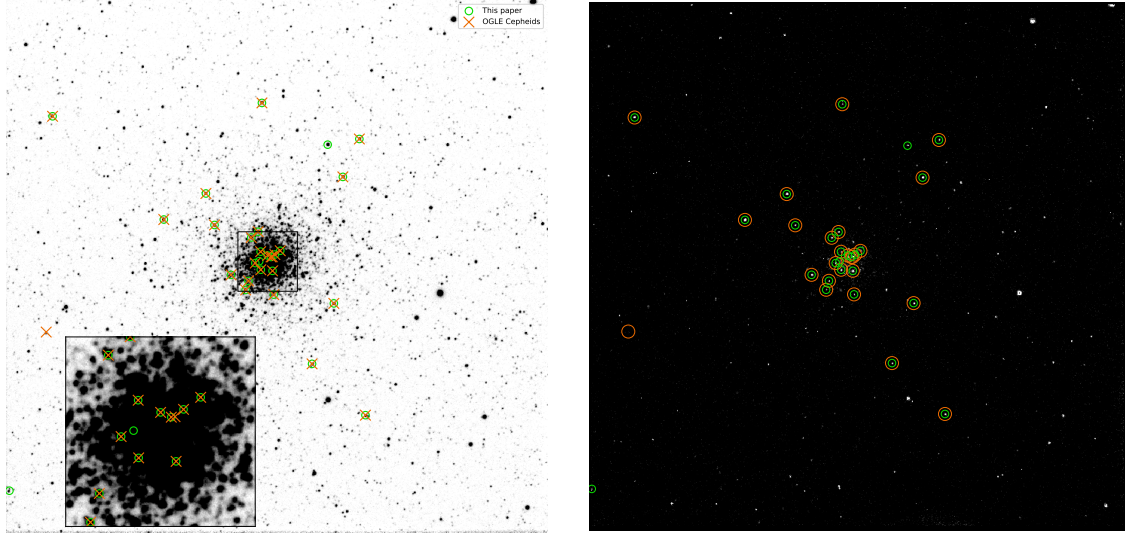


Figure 15. Comparing sources from the OGLE collection of variable stars to my detected sources.

This is far from the first study of Cepheid stars in NGC 1866, with [Storm et al. \(1988\)](#) reporting ten candidates, a number expanded upon by [Welch et al. \(1991\)](#) and [Welch & Stetson \(1993\)](#), bringing the number to around 23 by the time the Optical Gravitational Lensing Experiment (OGLE) completed its nearly definitive catalogue of classical Cepheids in the Large and Small Magellanic clouds ([Soszyński et al. 2017](#)). As the OGLE catalogue is the most complete census of Cepheid variable stars in the LMC to date, I compared my detections to the OGLE catalogue sources. My processing resulted in 27 putative Cepheid detections that passed my periodicity threshold. Note that these candidates were not vetted by examining the light curve shape, and so were assumed to be Cepheids based purely on having a period in the right range. The OGLE collection of classical Cepheids⁶ returns 26 sources within my field of view. Figure 15 shows my detections and the OGLE sources plotted together. While the OGLE sources are by and large a subset of my detections, there are two OGLE sources that have no counterparts in my data. On closer inspection, one of these sources is in my dataset, however the detected period did not score well enough to be included in my final sample. One OGLE source however is completely absent from my data. Looking at the plot on the right in Figure 15, which shows the OGLE detections and the detections from this paper over a difference image, we can see that there is one OGLE source that has no visible counterpart in my difference image. Examining the OGLE source, I suspect this is due to the faintness of the target, as

⁶ <http://ogledb.astrow.u.edu.pl/> ogle/OCVS/

the V- and I-band magnitudes reported by the OGLE survey show that this source is fainter than any of the sources I succeeded in detecting.

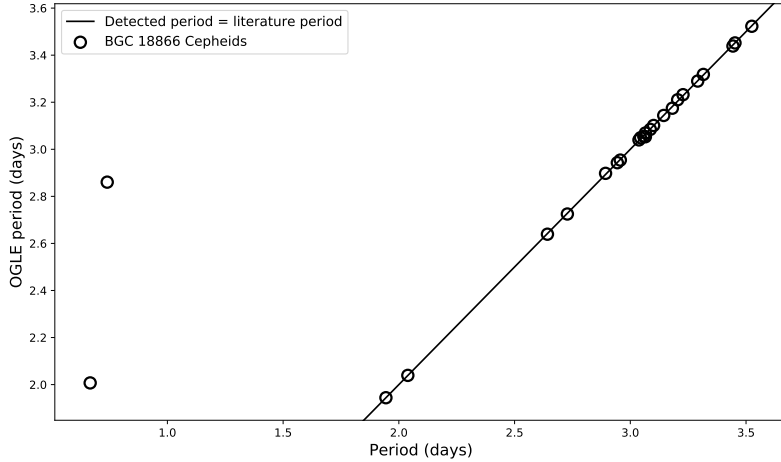


Figure 16. Period comparison with the OGLE survey (Soszyński et al. 2015).

Figure 16 compares the calculated periods for the sources detected both in this work and by the OGLE survey (Soszyński et al. 2015). The line of equality shown on the plot indicates that all but two of the periods calculated in this work agree very well with the OGLE values. Figure 17 shows the Lomb-Scargle periodogram for the two anomalous sources. We can see that in both cases the period I detected is an alias of the OGLE period, and that my scoring algorithm unfortunately scored the incorrect period higher than the correct one. It is of course possible that the OGLE period is the incorrect one, however, given the relative rigorousness of my period-finding algorithm vs. OGLE's, it is vastly more likely that mine is the period in error, particularly as the OGLE periods are more in line with normal classical Cepheid periods. Figure 18 shows the two outliers phased by my period and by the OGLE period. By eye, the fit of both periods appears roughly the same, which is expected given the similar height of the peaks in the periodograms, so it is not surprising that my somewhat naive period finding algorithm mistook an alias for the true period.

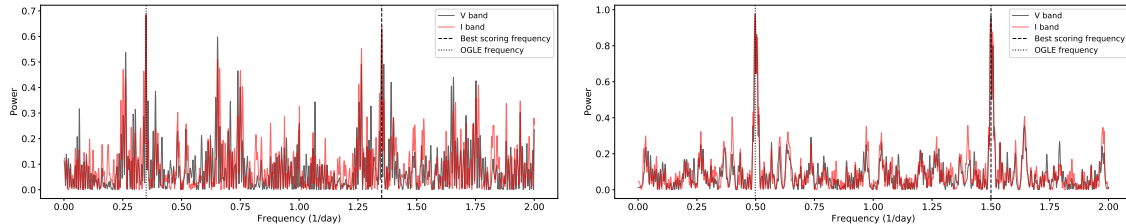


Figure 17. Periodograms in the I- and V-bands (red and black respectively) for the two sources whose periods as determined by this work diverge from those reported by the OGLE survey (Soszyński et al. 2015).

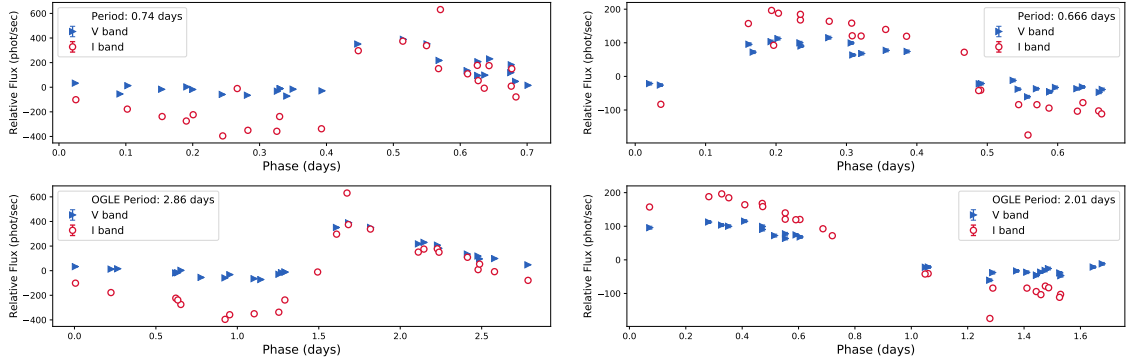


Figure 18. Light curves phased by the current work’s period and the OGLE period for the two sources whose periods as determined by this work diverge from those reported by the OGLE survey (Soszyński et al. 2015).

Table 2. NGC 1866 properties.

Reference	log (age/yr)	Distance (mag)	E(B-V)	Metallicity (Z)
This work	8.10	18.68	0.073	0.008
Bastian & Silva-Villa (2013); Marconi & Clementini (2005)	8.35	18.54 ± 0.02	0.09 – 0.12	0.008
McLaughlin & van der Marel (2005)	8.12	18.9	0.18	0.004
Brocato et al. (2003); Walker et al. (2001)	8.15 ± 0.1	18.35 ± 0.05	0.06 ± 0.005	0.007
Dupree et al. (2017)	8.15 and 8.3	18.31	0.11	0.006
Molinaro et al. (2012)		18.51 ± 0.01	0.06 ± 0.02	0.005
Storm et al. (2005)		18.30 ± 0.05	0.06 ± 0.01	0.004
Salaris et al. (2003) (MS fitting) (Red clump technique)		18.33 ± 0.08	0.064 ± 0.011	0.004 ± 0.0008
		18.53 ± 0.07	0.05 ± 0.02	0.004 ± 0.0008

4.2. NGC 1866 cluster age and distance

Table 2 contains a selection of literature values for for the age, distance, reddening, and metallicity of NGC 1866. I include the metallicity even though this work simply fixed it at $Z = 0.008$ because various parameters are sensitive to metallicity and it is thus important for understanding the results. As we can see from the table, my results are more or less in line with literature values, with my age being a bit on the low side and my distance modulus a bit on the high side. I simultaneously fit $\log(\text{age}/\text{yr})$, distance, and extinction, which yielded the results shown in the table. However if I fix the extinction at $E(B - V) = 0.06 \pm 0.005$ mag, one of the most commonly quoted values in the literature I then get $\log(\text{age}/\text{yr}) = 8.15$ and distance = 18.6 mag. This puts the age more in line with literature values, but the distance is still higher than literature estimates, particularly the ones that use main-sequence fitting (Salaris et al. 2003; Walker et al. 2001) which is the technique I used.

Table 3. Cepheid period-age relations ($\log t = \alpha + \beta \log P$) from literature.

Reference	α	β
This work	8.73 ± 0.05	-0.82 ± 0.07
Bono et al. (2005)	8.49 ± 0.09	-0.79 ± 0.01
Magnier et al. (1997)	8.4	-0.6
Efremov & Elmegreen (1998)	8.492	-0.677
Joshi & Joshi (2014)	8.6 ± 0.07	-0.77 ± 0.08
Anderson et al. (2016)	8.628	-0.665

4.3. Cepheid period-age relation

Table 3 and Figure 19 compare the Cepheid period-age relation ($\log t = \alpha + \beta \log P$) derived in this work with other values from the literature. While the α and β values derived in this work are higher than any of the literature values, they do agree within the error bounds. This is most obvious looking at figure 19 where we can see that while the position and slope of the period-age relations vary, they all group together, and the ones with stated error bars frame the entire collection.

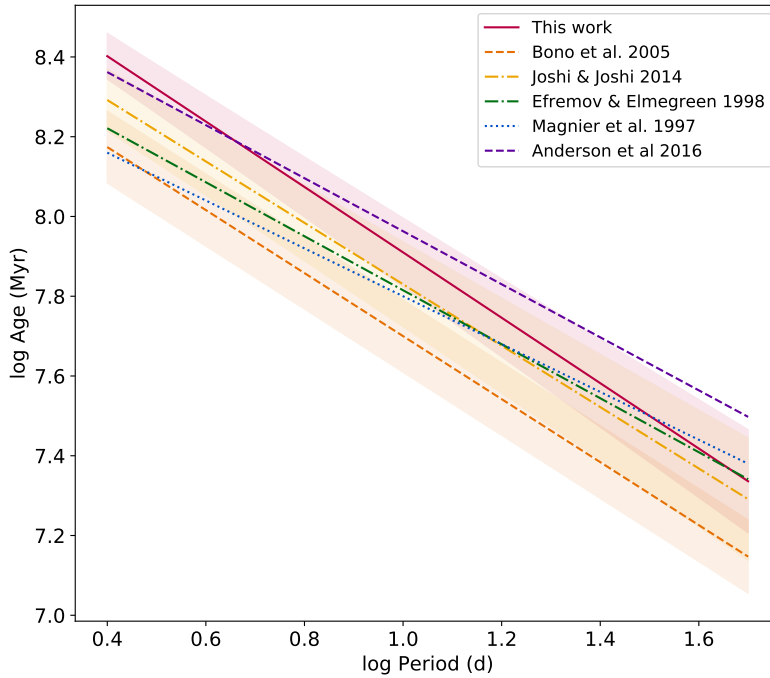


Figure 19. Cepheid period-age relations from a number of different sources.

There are a number of factors that affect the period-age determination, and can affect the accuracy of the results, I will talk about three of them here: metallicity, stellar rotation, and pulsation mode. Up to this point in this study I have more or

less ignored metallicity. I made a note of it when comparing age and distance values from the literature, but made no attempt to fit metallicity in my own calculations instead fixing it at $Z = 0.008$. However, as explored by [Bono et al. \(2005\)](#), chemical composition changes the period-age relation significantly. When comparing period-age relations, I used [Bono et al. \(2005\)](#)'s relation for $Z = 0.004$, while the relation reported by [Magnier et al. \(1997\)](#) was derived using Cepheids in M31, with ages fit to solar metallicity ($Z = 0.013$) isochrones despite the somewhat higher metallicity of M31. [Efremov & Elmegreen \(1998\)](#) used Cepheids from a variety of sources without reference to chemical composition, while [Joshi & Joshi \(2014\)](#) use only LMC clusters, with assumed metallicity $Z = 0.008$. In this study I am also using only LMC clusters, so my derived period-age relation is most comparable to that of [Joshi & Joshi \(2014\)](#), which can indeed be seen in Table 3. However the age determinations used in my calculation do not all come from calculations using the same metallicity assumptions, with [Ahumada et al. \(2019\)](#) reporting $Z = 0.014$ for NGC 1818, [Milone et al. \(2018\)](#) using $Z = 0.006$, [Niederhofer et al. \(2015\)](#) using $Z = 0.005$ and $Z = 0.008$, and this study using $Z = 0.008$. So this may in part explain some of the period-age relation discrepancies.

Stellar rotation has a complex affect on the period-age relation ([Anderson et al. 2016](#)). A Cepheid's age will depend on its lifetime on the main sequence which in turn depends on its rotation history. This effect is fairly straightforward: the faster a star's initial rotation, the longer its main-sequence lifetime and therefore the older it is as it enters its Cepheid phase. However, the relationship between period and rotation is more complex because while period is proportional to luminosity (the famous Cepheid period-luminosity relation), luminosity is affected by rotation, but is not directly proportional to it ([Anderson et al. 2016](#)). Thus rotation models affect the period-age relation, but not in an easily quantified way. The period-age relation from [Anderson et al. \(2016\)](#) shown in figure 19 assumes the average initial rotation rate ($\omega = 0.5$), and we can see that this relation does depart somewhat from the rest of the relations. Additionally, rotation has been suggested as a solution to the apparent existence of multiple stellar populations with different ages in stellar clusters ([Niederhofer et al. 2015; Bastian & de Mink 2009](#)). Features in the HR diagram of these clusters can be interpreted as age spreads on the order of 100 – 500 Myr, which would necessitate the separation of cluster Cepheids by age for an accurate period-age relation determination ([Niederhofer et al. 2015](#)). However stellar rotation in intermediate mass stars can also mimic this affect ([Bastian & de Mink 2009](#)).

The last complication I will discuss is that of pulsation modes. Cepheids can pulsate in the fundamental mode or at higher modes. Most period-age relations are derived for the fundamental mode, although [Bono et al. \(2005\)](#) derived period-age relations for both the fundamental mode and the first overtone. It is essential to include Cepheids of the same overtone only in a period-age relation, and to specify the overtone for which the relation holds. Returning to the OGLE catalogue sources

that correspond to my own detections, there are three sources that OGLE identifies as pulsating in the first overtone and which should be removed from my sample for calculating the average period used in the period-age relation derivation (Soszyński et al. 2015).

Given these considerations and the discussion in §4.2 about the NGC 1866 age determination, I recalculated the Cepheid fundamental mode period-age relation using the age $8.15 \log(\text{age}/\text{yr})$ and removing the non-fundamental mode Cepheids from the average period calculation. There is still some spread due to the different metallicity assumptions, however all of the clusters used in this relation are LMC clusters, so the metallicity spread is smaller than if Cepheids from other galaxies had been included. Redoing this calculation leads to the adjusted period-age relation $\log t = (8.54 \pm 0.11) - (0.64 \pm 0.17) \log P$ (Figure 20 left). This relation is somewhat different than the uncorrected version, but still in line with literature relations (see Figure 20 right). As a final note on this calculation, the age difference with and without fixing the reddening is small enough to have negligible affect on the period-age relation determination, instead the change in the relation is entirely an affect of the different average period for the cluster with the overtone Cepheids and false Cepheid detections removed.

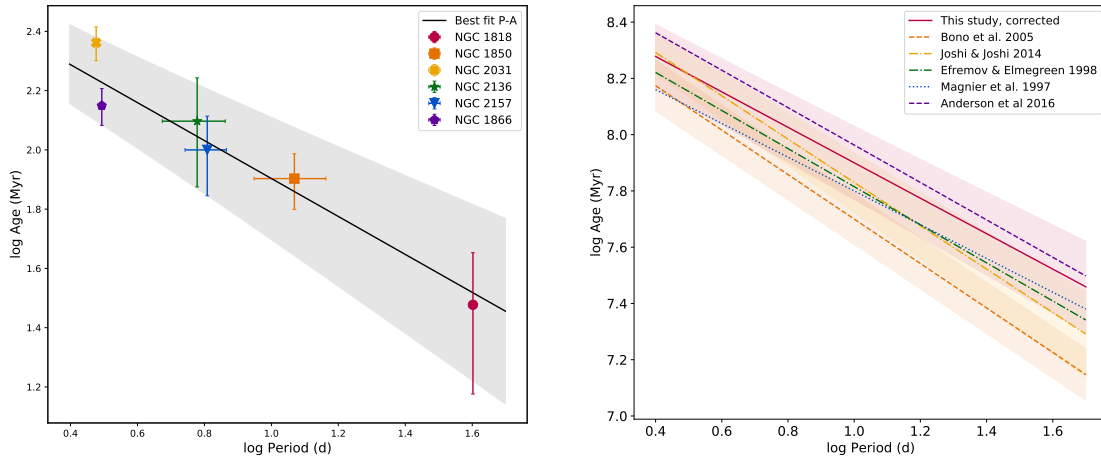


Figure 20. Cepheid period-age relation using only Cepheid fundamental mode Cepheids (left) and comparison of the relation with literature relations (right).

5. CONCLUSION

In this study I have performed a difference image search for variable stars in NGC 1866, extracted light curves, and performed period detection resulting in a collection of 27 putative Cepheid variable stars, with periods ranging from 0.5 – 51.5 days, with most periods clustering around ~ 3 days. I used the main sequence turn-off fitting technique to determine the age of the cluster, and combined my results with literature values for other LMC clusters to derive the Cepheid fundamental mode period-age

relation,

$$\log t = (8.54 \pm 0.11) - (0.64 \pm 0.17) \log P \quad (9)$$

where t is the age in years and P is the period in days.

I compared my result to literature values and found them to be broadly in agreement. I considered various sources of uncertainty and discussed their possible affect on my result. A more nuanced treatment of the problem would consider chemical composition and the effects of initial rotation rates, however even without these refinements my derived period-age relation is plausible and particularly similar to other results specifically using LMC Cepheids (e.g. [Joshi & Joshi \(2014\)](#)) a population that share more similar chemical compositions than Cepheids in other galaxies.

This work could be expanded to include a more in depth exploration of the location of the individual Cepheids in this sample within the classical instability strip, and potentially a study of the Cepheid period-luminosity relation, by cross-matching the HST photometric measurements of NGC 1866 with the population of detected Cepheids. Unfortunately the HST data did not have associated astrometry to allow that cross-match to take place. This exploration would not change the current results but would have allowed for a direct connection between the Cepheid period-age and period-luminosity relations on the same population of Cepheids. Additionally both the period-age, and period-luminosity relations have colour components that were not discussed in this work and would be a natural avenue for future exploration.

Several major all-sky time-domain surveys are in progress (TESS, Pan-STARRS) or coming online in the next few years (LSST), creating unprecedented opportunities to find and study many time-varying astronomical phenomena including variable stars. This study used a relatively small number of observations to explore the population of Cepheid stars present in NGC 1866 and was able to very accurately determine the periods of most of the known NGC 1866 Cepheids. Large scale all-sky surveys offer a much higher data rate, if less specifically targeted, and thus offer the opportunity to refine the parameters of known variables, discover previously undetected variables, and observe how variable sources evolve over time. The rate of change of a Cepheid's period is related to its instability strip crossing mode, a property that can be used to place the star within the instability strip ([Turner et al. 2006](#)). This in turn can help constrain the Cepheid's evolution and put limits on stellar evolution models. Long-term all-sky surveys offer the opportunity to make these Cepheid period evolution measurements for a large number of Cepheid stars, helping to map the stellar evolution of the Milky Way and other nearby galaxies.

A huge thank you to my project advisor David Bersier, and Nathan Bastien at Liverpool John Moores University for supporting this project from start to finish. Thanks also to Erik Tollerud, Susan Mullally, and David Rodriguez at the Space Telescope Science Institute for Python help, answering many questions, and generally being willing to chat about data reduction and photometry. And thank you as well to Ri Turner and Jane Anderson, who gamely listened to me explain my project and asked thoughtful questions despite not being astronomers.

This research made use of ccdproc, an Astropy package for image reduction ([Craig et al. 2015](#)).

This work has made use of data from the European Space Agency (ESA) mission *Gaia* (<https://www.cosmos.esa.int/gaia>), processed by the *Gaia* Data Processing and Analysis Consortium (DPAC, <https://www.cosmos.esa.int/web/gaia/dpac/consortium>). Funding for the DPAC has been provided by national institutions, in particular the institutions participating in the *Gaia* Multilateral Agreement.

This research is based in part on observations made with the NASA/ESA Hubble Space Telescope obtained from the Space Telescope Science Institute, which is operated by the Association of Universities for Research in Astronomy, Inc., under NASA contract NAS 526555. These observations are associated with program GO-14069.

Facilities: Las Cumbres Observatory, Siding Spring Observatory (FTS), Hubble Space Telescope (WFC3/UVIS)

Software: Astropy ([Astropy Collaboration et al. 2013](#)), Astroquery ([Ginsburg et al. 2019](#)), SaoImage DS9 ([Joye & Mandel 2003](#)), hotpants ([Becker 2015](#)), Matplotlib ([Hunter 2007](#)), ccdproc ([Craig et al. 2015](#)), reproject ([Robitaille 2018](#)), brokenaxes (github.com/bendichter/brokenaxes)

APPENDIX

A. DETECTED CEPHEID PERIODS

Table 4. All detected variable stars in NGC 1866 whose periodicity passed the threshold to be considered periodic. The OGLE Cepheid detection that did not pass the threshold is also included.

ID	RA (deg)	Dec (deg)	Period (d)	Score			
ID	RA	Dec	x	y	period	score	
5	78.41662	-65.51458	965.89	387.46	2.04	-6.93	
6	78.57644	-65.50981	173.82	438.04	3.20	-5.01	
7	78.34207	-65.50335	1334.51	523.85	3.14	-7.03	
8	78.36624	-65.50149	1214.66	545.41	51.52	-5.71	
9	78.35453	-65.49132	1272.11	667.32	2.64	-7.49	
11	78.45895	-65.48578	754.02	730.07	2.96	-7.72	
13	78.49094	-65.47743	594.70	828.61	3.44	-5.41	
15	78.45223	-65.47582	786.55	849.25	3.10	-6.10	
17	78.41893	-65.47378	951.60	874.79	3.04	-6.97	
18	78.42415	-65.47194	925.56	896.65	1.94	-6.25	
20	78.40199	-65.46781	1035.25	946.71	3.07	-5.74	
21	78.41694	-65.46748	961.02	950.14	3.04	-6.20	
22	78.40608	-65.46660	1014.87	961.03	3.29	-6.45	
23	78.41156	-65.46629	987.67	964.60	3.07	-5.76	
25	78.40900	-65.46582	1000.34	970.28	3.18	-5.51	
26	78.40810	-65.46587	1004.79	969.72	2.89	-4.59	
29	78.41800	-65.46446	955.56	986.25	1.01	-5.49	
31	78.42097	-65.46386	940.79	993.29	3.06	-7.41	
34	78.41674	-65.46175	961.61	1018.61	0.74	-5.22	
35	78.40778	-65.46143	1006.07	1022.74	3.23	-7.15	
36	78.43945	-65.46006	848.81	1038.04	2.73	-6.99	
37	78.42609	-65.45819	914.96	1060.90	3.45	-7.36	
38	78.42817	-65.45532	904.46	1095.12	0.67	-6.44	
40	78.40673	-65.45391	1010.76	1112.71	3.32	-6.23	
41	78.36093	-65.45125	1238.01	1145.95	3.52	-6.64	
43	78.37729	-65.43206	1155.60	1374.74	3.09	-7.67	
44	78.33645	-65.41591	1357.60	1568.81	2.94	-6.82	
49	78.60688	-65.39113	10.50	1854.64	0.63	-6.55	

B. DETECTED CEPHEID PHASED LIGHT CURVES

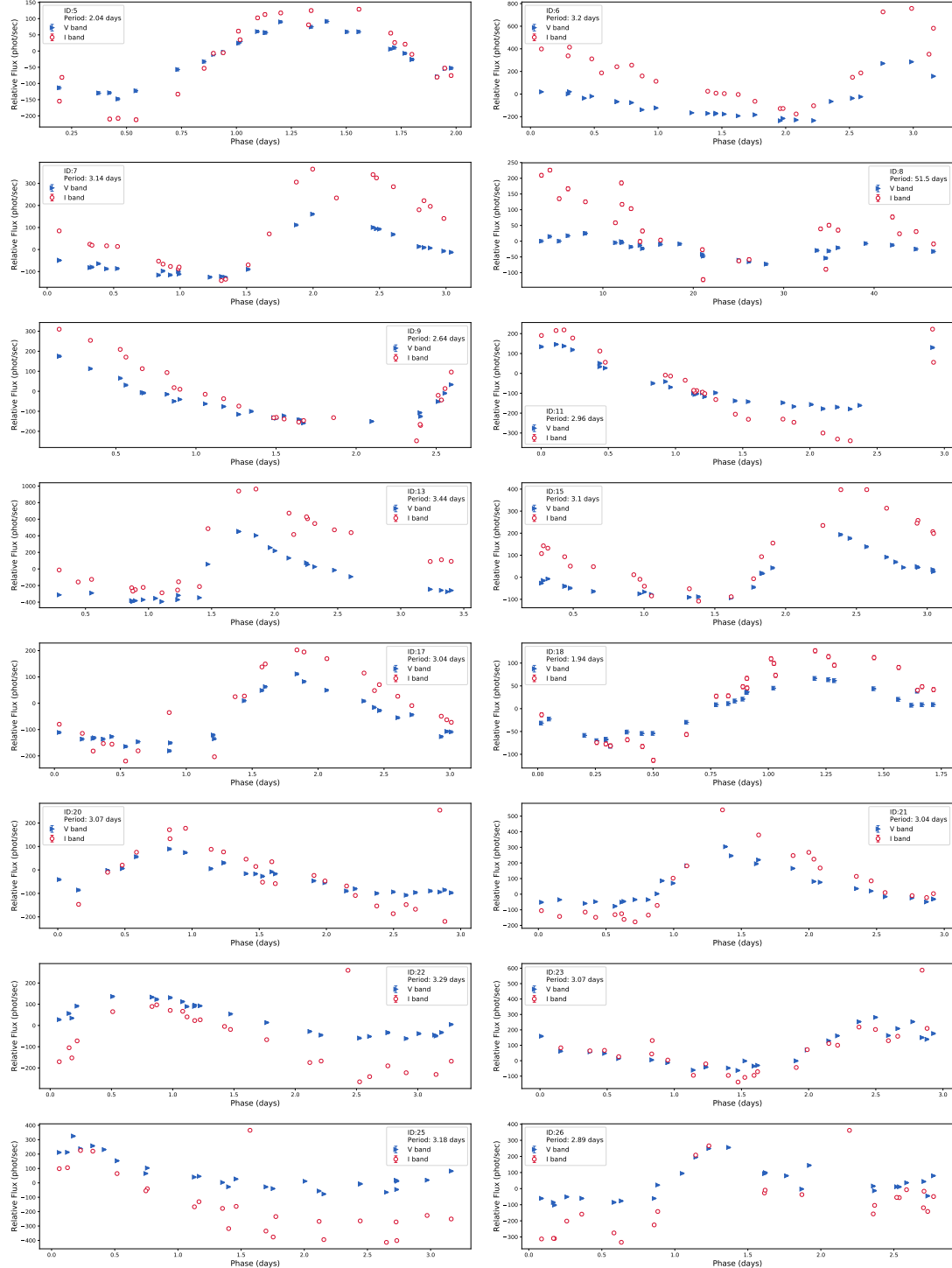


Figure 21. Phased light curves for all detected variable stars in NGC 1866 whose periodicity passed the threshold to be considered periodic. The OGLE Cepheid detection that did not pass the threshold is also included.

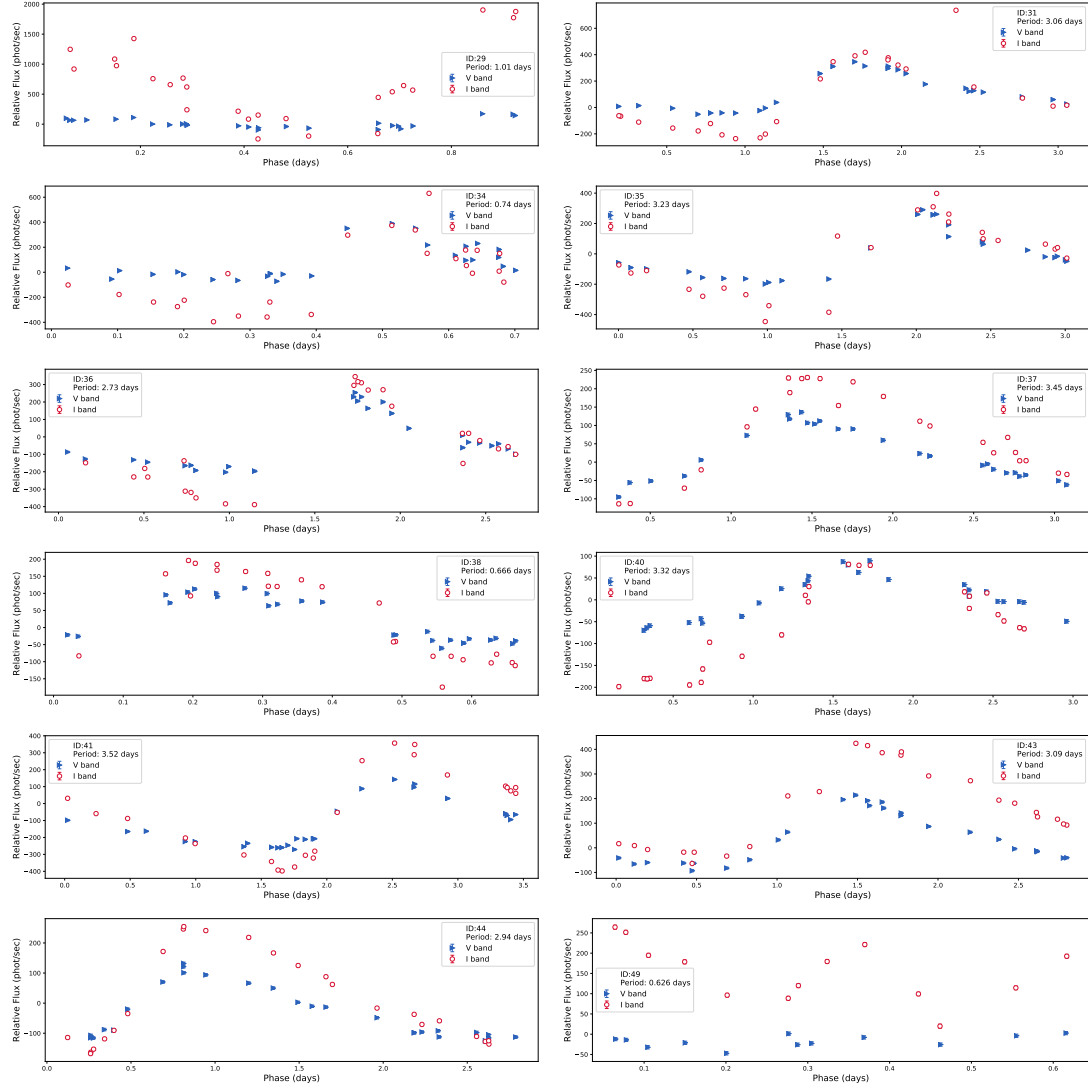


Figure 21 (cont). Phased light curves for all detected variable stars in NGC 1866 whose periodicity passed the threshold to be considered periodic. The OGLE Cepheid detection that did not pass the threshold is also included.

REFERENCES

- Ahumada, A. V., Vega-Neme, L. R., Clariá, J. J., & Minniti, J. H. 2019, PASP, 131, 024101
- Alard, C. 2000, A&AS, 144, 363
- Alard, C., & Lupton, R. H. 1998, ApJ, 503, 325
- Anderson, J., & King, I. R. 2006, PSFs, Photometry, and Astronomy for the ACS/WFC, Tech. rep.
- Anderson, R. I., Saio, H., Ekström, S., Georgy, C., & Meynet, G. 2016, Astronomy and Astrophysics, 591, A8
- Astropy Collaboration, Robitaille, T. P., Tollerud, E. J., et al. 2013, A&A, 558, A33
- Barmina, R., Girardi, L., & Chiosi, C. 2002, Astronomy and Astrophysics, 385, 847
- Bastian, N., & de Mink, S. E. 2009, MNRAS, 398, L11
- Bastian, N., & Silva-Villa, E. 2013, MNRAS, 431, L122
- Becker, A. 2015, HOTPANTS: High Order Transform of PSF AND Template Subtraction, , ascl:1504.004

- Bono, G., Marconi, M., Cassisi, S., et al. 2005, *ApJ*, 621, 966
- Bradley, L., Sipocz, B., Robitaille, T., et al. 2016, Photutils: Photometry tools, , , ascl:1609.011
- Bressan, A., Marigo, P., Girardi, L., et al. 2012, *MNRAS*, 427, 127
- Brocato, E., Castellani, V., Di Carlo, E., Raimondo, G., & Walker, A. R. 2003, *AJ*, 125, 3111
- Chen, Y., Girardi, L., Bressan, A., et al. 2014, *MNRAS*, 444, 2525
- Craig, M. W., Crawford, S. M., Deil, C., et al. 2015, ccdproc: CCD data reduction software, , , ascl:1510.007
- Devor, J. 2005, *ApJ*, 628, 411
- Dupree, A. K., Dotter, A., Johnson, C. I., et al. 2017, *ApJL*, 846, L1
- Efremov, Y. N., & Elmegreen, B. G. 1998, *MNRAS*, 299, 588
- Fitzpatrick, E. L. 1999, *PASP*, 111, 63
- Gaia Collaboration, Prusti, T., de Bruijne, J. H. J., et al. 2016, *A&A*, 595, A1
- Gaia Collaboration, Brown, A. G. A., Vallenari, A., et al. 2018, *A&A*, 616, A1
- Ginsburg, A., Sipócz, B. M., Brasseur, C. E., et al. 2019, *AJ*, 157, 98
- Hartman, J. D., & Bakos, G. Á. 2016, *Astronomy and Computing*, 17, 1
- Hunter, J. D. 2007, *Computing in Science and Engineering*, 9, 90
- Joshi, Y. C., & Joshi, S. 2014, *NewA*, 28, 27
- Joye, W. A., & Mandel, E. 2003, in *Astronomical Society of the Pacific Conference Series*, Vol. 295, *Astronomical Data Analysis Software and Systems XII*, ed. H. E. Payne, R. I. Jedrzejewski, & R. N. Hook, 489
- Leavitt, H. S., & Pickering, E. C. 1912, *Harvard College Observatory Circular*, 173, 1
- LeBlanc, F. 2010, An Introduction to Stellar Astrophysics
- Magnier, E. A., Prins, S., Augusteijn, T., van Paradijs, J., & Lewin, W. H. G. 1997, *A&A*, 326, 442
- Marconi, M., & Clementini, G. 2005, *AJ*, 129, 2257
- Marconi, M., Molinaro, R., Ripepi, V., Musella, I., & Brocato, E. 2013, *Monthly Notices of the Royal Astronomical Society*, 428, 2185
- McLaughlin, D. E., & van der Marel, R. P. 2005, *ApJS*, 161, 304
- Milone, A. P., Marino, A. F., Di Criscienzo, M., et al. 2018, *MNRAS*, 477, 2640
- Molinaro, R., Ripepi, V., Marconi, M., et al. 2012, *ApJ*, 748, 69
- Musella, I., Marconi, M., Stetson, P. B., et al. 2016, *Monthly Notices of the Royal Astronomical Society*, 457, 3084
- Niederhofer, F., Hilker, M., Bastian, N., & Silva-Villa, E. 2015, *A&A*, 575, A62
- Niederhofer, F., Bastian, N., Kozhurina-Platais, V., et al. 2017, *MNRAS*, 464, 94
- Robitaille, T. 2018, Reproject: Astronomical Image Reprojection In Python, v0.4, Zenodo, doi:10.5281/zenodo.1162674
- Salaris, M., Percival, S., Brocato, E., Raimondo, G., & Walker, A. R. 2003, *ApJ*, 588, 801
- Schwarzenberg-Czerny, A. 1989, *MNRAS*, 241, 153
- Skowron, D. M., Skowron, J., Mróz, P., et al. 2019, *Science*, 365, 478
- Sosey, M. 2017, Imexam Version 0.8.0 Release, v0.8.0, Zenodo, doi:10.5281/zenodo.1042809
- Soszyński, I., Udalski, A., Szymański, M. K., et al. 2015, *Acta Astronomica*, 65, 297
- . 2017, *Acta Astronomica*, 67, 103
- Stetson, P. B. 1987, *PASP*, 99, 191
- Storm, J., Andersen, J., Blecha, A., & Walker, M. F. 1988, *Astronomy and Astrophysics*, 190, L18
- Storm, J., Gieren, W. P., Fouqué, P., Barnes, T. G., I., & Gómez, M. 2005, *A&A*, 440, 487
- Tang, J., Bressan, A., Rosenfield, P., et al. 2014, *MNRAS*, 445, 4287
- Turner, D. G. 2012, *Journal of the American Association of Variable Star Observers (AAVSO)*, 40, 502

- Turner, D. G., Abdel-Sabour Abdel-Latif, M., & Berdnikov, L. N. 2006, PASP, 118, 410
- VanderPlas, J., Connolly, A. J., Ivezić, Z., & Gray, A. 2012, in Proceedings of Conference on Intelligent Data Understanding (CIDU, 47–54
- VanderPlas, J. T. 2018, ApJS, 236, 16
- VanderPlas, J. T., & Ivezić, Ž. 2015, ApJ, 812, 18
- Walker, A. R., Raimondo, G., Di Carlo, E., et al. 2001, ApJL, 560, L139
- Welch, D. L., Mateo, M., Cote, P., Fischer, P., & Madore, B. F. 1991, The Astronomical Journal, 101, 490
- Welch, D. L., & Stetson, P. B. 1993, The Astronomical Journal, 105, 1813
- Young, A. T. 1962, PhD thesis, Harvard University